Enhanced Electrochemical H_2 Evolution by Few-Layered Metallic $WS_{2(1-x)}Se_{2x}$ Nanoribbons

*Fengmei Wang, Jinshan Li, Feng Wang, Tofik Ahmed Shifa, Zhongzhou Cheng, Zhenxing Wang, Kai Xu, Xueying Zhan, Qisheng Wang, Yun Huang, Chao Jiang, and Jun He**

As an effective alternative to noble platinum electrocatalyst, earth abundant and inexpensive layered transition metal dichalcogenides (TMDs) are investigated for the hydrogen evolution reaction (HER). Compared with binary TMDs, the tunably composed ternary TMDs have hitherto received relatively little attention. Here, few-layered ternary $WS_{2(1-x)}Se_{2x}$ nanoribbons (NRs) with metallic 1T phases, much more catalytically active in HER, are prepared for the first time. The favorable $\Delta G_H°$ introduced by the tensile region on the surface, along with the presence of local lattice distortions of the $WS_{2(1-x)}Se_{2x}$ nanoribbons with metallic 1T phases, greatly promotes the HER process. These ternary NRs achieve the lowest overpotential of ≈0.17 V at 10 mA cm^{-2} and a Tafel slope of ≈68 mV dec^{-1} at a low catalyst loading (≈0.30 ± 0.02 mg cm^{-2}). Notably, the long-term durability suggests the potential of practical applications in acid electrolytes. The results here suggest that the ternary $WS_{2(1-x)}Se_{2x}$ NRs with 1T phases are prominent alternatives to platinum-based HER electrocatalysts.

1. Introduction

With the increasing environmental pollution resulted from fossil fuel, clean energy hydrogen fuel has attracted intense research recently. The hydrogen evolution reaction (HER), as a fundamental step of electrochemical water splitting, offers a promising and sustainable solution to produce H_2 through the transformation of the electrical energy into chemical energy.[1] A favorable electrocatalyst can promote the conversion from two protons to H_2 ($2H^+ + 2e^- \rightarrow H_2$) at high reaction rates and low overpotential (η). Precious metal platinum (Pt) and its alloys meet the aforementioned requirements and act as excellent electrocatalysts in HER process.[2,3] However, prohibitive cost and scarcity of Pt hinder the widespread practical application. Presently, the possibility of using earth abundant and inexpensive binary layered transition metal dichalcogenides (TMDs),[4] such as MoS_2,[5–7] WS_2,[8–10] $MoSe_2$,[11–14] and WSe_2,[11,12] in HER have been investigated. Experimental and theoretical studies indicate that the (10–10) planes on edges of MoS_2, WS_2, and WSe_2 are catalytically active for HER due to the low Gibbs free energy for hydrogen absorption ($\Delta G_H°$), while the (0001) basal planes are catalytically inert.[6] Enormous attempts, thus, have been taken to synthesize lamellar binary layered TMDs exploring lots of edges.[13,15,16] To further improve the HER activity of these TMDs, many researchers made great effort to optimize $\Delta G_H°$ through regulating the chemical composition. For example, introducing Co, Fe, and Ni cations[17] into the TMD-based electrocatalysts has been conducted. The improvement results from the reduced $\Delta G_H°$ of the edge, which increases the absorbed H coverage and promotes the catalytic activity of active sites.[3,17,18] Analogously, TMDs with ternary component, such as $MoS_{2(1-x)}Se_{2x}$[19,20] and MoS_xCl_y,[21] are also studied in HER. These composition tunable TMDs demonstrate a better HER performance than their binary counterparts due to the proliferation of unsaturated HER active sites. However, the preparation of composition tunable nanostructures in high yields that are amenable to electrocatalytic application is currently lacking. And compared with the binary ones, the ternary TMDs received relatively little attention, especially for $WS_{2(1-x)}Se_{2x}$. In addition to varying their composition, the electroactivity of TMDs can be tuned by altering their electronic structure. Some researches show higher HER activities are realized for the MoS_2[22] and WS_2[8,9] with 1T phase than that with 2H phase. The appropriate strained metallic 1T phase existed on the surface can positively influence $\Delta G_H°$, resulting

F. M. Wang, F. Wang, T. A. Shifa, Z. Cheng, Prof. Z. Wang, K. Xu, X. Zhan, Q. Wang, Y. Huang, Prof. J. He
CAS Key Laboratory of Nanosystem and Hierarchical Fabrication
National Center for Nanoscience and Technology
Beijing 100190, P. R. China
E-mail: hej@nanoctr.cn

F. M. Wang, F. Wang, T. A. Shifa, K. Xu, Q. Wang, Y. Huang
University of Chinese Academy of Sciences
Beijing 100049, P. R. China

J. Li
School of Chemistry and Chemical Engineering
University of Chinese Academy of Sciences
Beijing 100049, P. R. China

Prof. C. Jiang
CAS Key Laboratory of Standardization and Measurement for Nanotechnology
National Center for Nanoscience and Technology
Beijing 100190, P. R. China

DOI: 10.1002/adfm.201502680

in improving intrinsically the catalytic ability.[12] But, the composition tunable ternary TMDs with metallic 1T phase has seldom been investigated in HER catalysis.

Our group has recently demonstrated a facile way to prepare ternary $WS_{2(1-x)}Se_{2x}$ nanotubes (NTs) in high yields through converting WO_3 nanowires (NWs), and the composition of the NTs can be systematically tuned by the control of growth condition.[23] The layer dislocations and defects on the walls are crucial for electrochemical performance. However, the confined number of the exposed edge sites on the NTs hinder the electrocatalytic activity of $WS_{2(1-x)}Se_{2x}$. Besides, the electrons tend to transfer from the conductive carbon fibers (CFs) to the layer dislocations and defects existing on the walls of the NTs passing through the entire vertical NT. This increases the resistance in the process of the HER reaction. Herein, the laterally ultrathin ternary $WS_{2(1-x)}Se_{2x}$ nanoribbons (S NRs) are grown on the flexible CFs via simple process. Compared with the NTs, the NRs exhibit the improved electrocatalytic activity due to the increased concentration of exposed edges. Motivated by the active role of 1T phase in electrochemical catalysis, we performed experiments for in situ introduction of 1T phase into ternary NRs initially by the method of the lithium intercalation reaction. The few-layered composition tunable ternary $WS_{2(1-x)}Se_{2x}$ NRs with metallic 1T phase achieved the lowest overpotential of ≈0.17 V at 10 mA cm^{-2} and a Tafel slope of ≈68 mV dec^{-1}.

2. Results and Discussion

$WS_{2(1-x)}Se_{2x}$ NTs with a 2H phase (denoted as S NTs) were grown on the surface of CFs by simultaneously sulfurizing and selenizing WO_3 NWs as reported in our previous work (Figure S1a–d, Supporting Information, see the Experimental Section for details of synthesis).[23] The morphology of the NT was shown by means of transmission electron microscopy (TEM) in **Figure 1**a, exhibiting the multiwall nanotubes in (002) planes with the interlayer spacing of 0.641 nm. Then, the $WS_{2(1-x)}Se_{2x}$ NTs were unzipped for S NRs in the ethanol and deionized (DI) water solvent in autoclave at 170 °C (Figure S2a,b, Supporting Information). Unlike the NTs growing vertically, some NRs lied on the curved surface of CFs and contacted with the substrate directly. During this process, the layer dislocations and defects existing on the walls demonstrated in our reported work play an important role on the unzipping NTs to NRs under high temperature and pressure in the autoclave.[23] Figure 1b presents the TEM image of the NR with the diameter of ≈100 nm. Lattice-resolved high-resolution transmission electron microscopy (HRTEM) image shows highly crystalline few-layered ribbons (Figure 1e). The X-ray diffraction (XRD) patterns reveal that there is a subtle shift of the (002) plane in ternary $WS_{2(1-x)}Se_{2x}$ NTs compared to 2H-WS_2 (PDF #08-0237) and 2H-WSe_2 (PDF #06-0080). The simultaneous incorporation of S and Se atoms during the formation

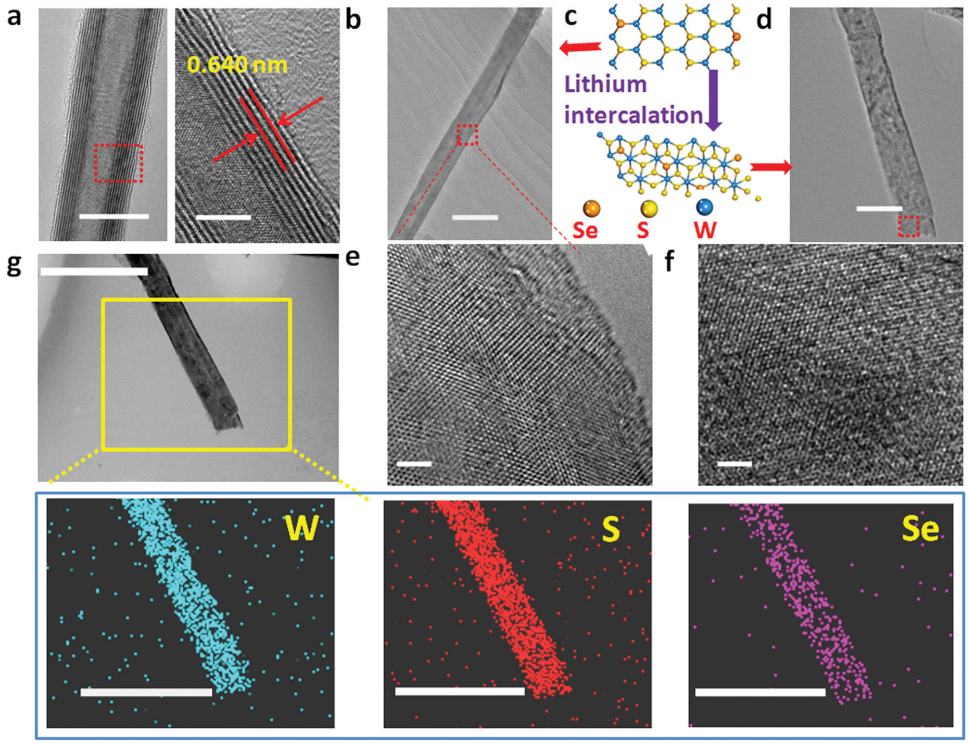

Figure 1. Characterization of $WS_{2(1-x)}Se_{2x}$ ($x \approx 0.22$) NRs after intercalation with *n*-butyl lithium (denoted S NRs-Li). a) TEM images with different magnifications of the $WS_{2(1-x)}Se_{2x}$ ($x \approx 0.22$) NTs. Scale bars 20 and 50 nm, respectively. b) TEM and e) HRTEM images of the $WS_{2(1-x)}Se_{2x}$ ($x \approx 0.22$) NRs. Scale bars 100 and 2 nm, respectively. c) A simple lithium intercalation process is used to drive the phase transformation from the 2H to the 1T $WS_{2(1-x)}Se_{2x}$ polymorph. d) TEM and f) HRTEM images with different magnifications of the S NR-Li. Scale bars, 100 and 2 nm, respectively, demonstrating more disordered structures in the HRTEM image. g) STEM-EDX elemental mapping of S NR-Li showing clearly the homogeneous distribution of W, S, and Se. Scale bars 500 nm.

of the ternary $WS_{2(1-x)}Se_{2x}$ NTs affects the interlayer distance. Compared with the binary ones, the change in the interlayer *d*-spacing of the ternary $WS_{2(1-x)}Se_{2x}$ NTs is due to the different size of S and Se. Thus, the observed slight shift in XRD (002) peak indicates the formation of a new lamellar structure.[24] Moreover, the broadened diffraction peak reflects the nanoscale dimensions of ternary $WS_{2(1-x)}Se_{2x}$ NTs. The phase identity of the as-exfoliated NRs is the same as the NTs with semiconducting 2H phase. Remarkably, the weak intensity of the (002) peak in the XRD pattern of the unzipped sample suggests diminishing of the long-range stacking order of the nanotubes along the *c*-axis, indicating the emergence of the few-layered NRs on CFs. This result is consistent with the reported work.[22] The 2H phase of the unzipped NRs was further confirmed using Raman spectroscopy in the subsequent analysis.

The lithium intercalation chemistry is usually utilized to control the structural polymorphs in some binary TMDs (MoS_2 and WS_2).[8,9,13,22] Modification of the crystal structure was induced through the electron transfer between the lithium compound (*n*-butyllithium) and the TMD nanostructures during the intercalation reaction,[25] resulting in emergence of coexistence of the two different phases (2H and 1T).[26] Meanwhile, the strain on the basal plane induced has been confirmed to have a positive influence on HER.[8] Here, the unzipped $WS_{2(1-x)}Se_{2x}$ NRs were initially transferred from semiconducting 2H phase to metallic 1T polymorph NRs (denoted as S NRs-Li) by heating the samples immersed in *n*-butyllithium solution at ≈50 °C with stirring for 16 h (Figure 1c). TEM image in Figure 1d presents that the NR morphology with the diameter of ≈100 nm was preserved, though the NRs-Li were compressed onto the surface of CFs (Figure S2c,d, Supporting Information). But, more disordered structures of the NR-Li were observed in HRTEM image (Figure 1f), which is common to develop during Li intercalation.[27] Energy-dispersive X-ray spectrum (EDX) elemental mappings of W, Se, and S from the marked detection range of the NR-Li (Figure 1g) suggest uniform and homogeneous distribution constituents across the nanoribbon. Additionally, EDX analysis in **Figure 2**a exhibits the atomic ratio of Se:S close to 0.44:1.56 for $WS_{2(1-x)}Se_{2x}$ where $x \approx 0.22$ (Cu and C peaks emanate from the carbon-coated TEM grid) (Table S1, Supporting Information). The atomic force microscopy (AFM) image of S NRs-Li (Figure 2b) further supports the TEM observations. A ≈4 nm thick NR-Li indicates the multilayer nanoribbons. Notably, some NRs-Li with the thickness of ≈1.3 nm also appeared, suggesting that the sample consists of few layers. Compared with the S NRs, the weaker intensity of the (002) peak in the XRD pattern (Figure S2e, Supporting Information) further confirms the ultrathin feature of NRs after Li intercalation. The reaction between Li-intercalated NRs and excess water further chemically exfoliates the NRs.

We further characterized the $WS_{2(1-x)}Se_{2x}$ NRs after Li intercalation to highlight their difference from the as-unzipped NRs using Raman spectroscopy and X-ray photoelectron spectroscopy (XPS). Raman spectra of all the samples (Figure 2c and Figure S3a, Supporting Information) were measured by an unpolarized 532 nm laser in backscattering geometry. The Raman spectrum of $WS_{2(1-x)}Se_{2x}$ NRs consists of band in the low wave number region (100–500 cm^{-1}), which is contributed by WS_2-like band and WSe_2-like band. The bands around 350 and 415 cm^{-1} are attributed to WS_2-like E^1_{2g} (in-plane) and A_{1g} (out-of-plane) modes, respectively. The other set at around 250 cm^{-1} is related to the corresponding WSe_2-like E^1_{2g}/2LA features.[23,28] For S NRs-Li, the emergence of new Raman shift at ≈124, ≈155, and ≈200 cm^{-1} in low frequency, similar to the case in chemically exfoliated MoS_2[22,29] and WS_2,[8,9] is associated with the phonon modes of $WS_{2(1-x)}Se_{2x}$ contained 1T phase. Moreover, the larger E^1_{2g}/A_{1g} ratio in S NRs-Li than that in S NR also indicates the formation of 1T phase.[8] The Raman spectrum of S NRs-Li confirms the coexistence of the 1T and 2H polymorphs in $WS_{2(1-x)}Se_{2x}$ NRs after Li intercalation. Furthermore, the structural transformations and the concentration of 1T and 2H were detected by XPS. The high-resolution core-level W 4f, S 2p, and Se 3p peaks were illustrated in Figure 2d,e. The peaks at 35.4 and 33.2 eV correspond to the W $4f_{5/2}$ and W $4f_{7/2}$ originating primarily from the native semiconducting 2H phase. Deconvolution analysis of these peaks in S NRs-Li sample reveals that they are shifted toward slightly lower energies (35.1 and 32.8 eV) compared to the 2H phase. Similar peak shifts are also found in the S 2p, Se 3p, and Se 3d peaks bisected with dotted line (Figure 2e and Figure S3b, Supporting Information). These results, in agreement with some reported results, elucidate the presence of 1T phase in few-layered NRs on CFs after Li intercalation.[8,9,13] XPS analysis of the NRs after Li intercalation exhibited the Se mole fraction *x* (= S/(S + Se)) of ≈0.23, consistent with the result of EDX analysis. Importantly, the C1s signal in the high-resolution XPS spectra (Figure S4, Supporting Information) remains unchanged as evidenced from S NTs and S NRs-Li features. This shows the chemical stability of CFs irrespective of the various solution treatments.

The HER electrochemical activities of the different NRs on CFs are evaluated directly in a standard three-electrode electrochemical cell setup with N_2-deaerated ≈0.5 M H_2SO_4 electrolyte at room temperature. For comparison, the WS_2 and WSe_2 NRs on CFs are also prepared with the same method (Figure S5, Supporting Information). The HER electrocatalytic activity of the binary NRs was investigated and compared with that of ternary $WS_{2(1-x)}Se_{2x}$ ($x \approx 0.22$) NRs in Figure S6 (Supporting Information), showing the best performance of the $WS_{2(1-x)}Se_{2x}$ ($x \approx 0.22$) NRs. Furthermore, this value is also better than some other reported binary MoS_2[30] and WSe_2 catalysts.[12] The plausible explanation for the improved HER performance of ternary NRs may be due to the more appropriate $\Delta G_H{}^o$ and increased active sites.[15,19,31]

As can be seen from **Figure 3**a, polarization curve after *iR* correction of the ternary unzipped $WS_{2(1-x)}Se_{2x}$ ($x \approx 0.22$) NRs displays ≈203 mV versus RHE, which is much lower than that of $WS_{2(1-x)}Se_{2x}$ ($x \approx 0.22$) NTs at same current density (≈235 mV at 10 mA cm^{-2}). The enhanced HER performance of S NRs is due to the following aspects: i) The higher concentration of electrocatalytic edges[6,32] is realized after unzipping the NTs to NRs. And the augment in the density of exposed active sites due to the exfoliation was revealed by ≈7-fold increase in the double layer capacitance (C_{dl}) from ≈1.27 up to ≈6.98 mF cm^{-2} (Figure S7, Supporting Information). ii) As shown in scanning electron microscope (SEM) images in Figure S2 (Supporting Information), the NRs entwine on the curved surface of CFs with improved electrical contact from the electrode to the active sites. Thus, the electrons can be

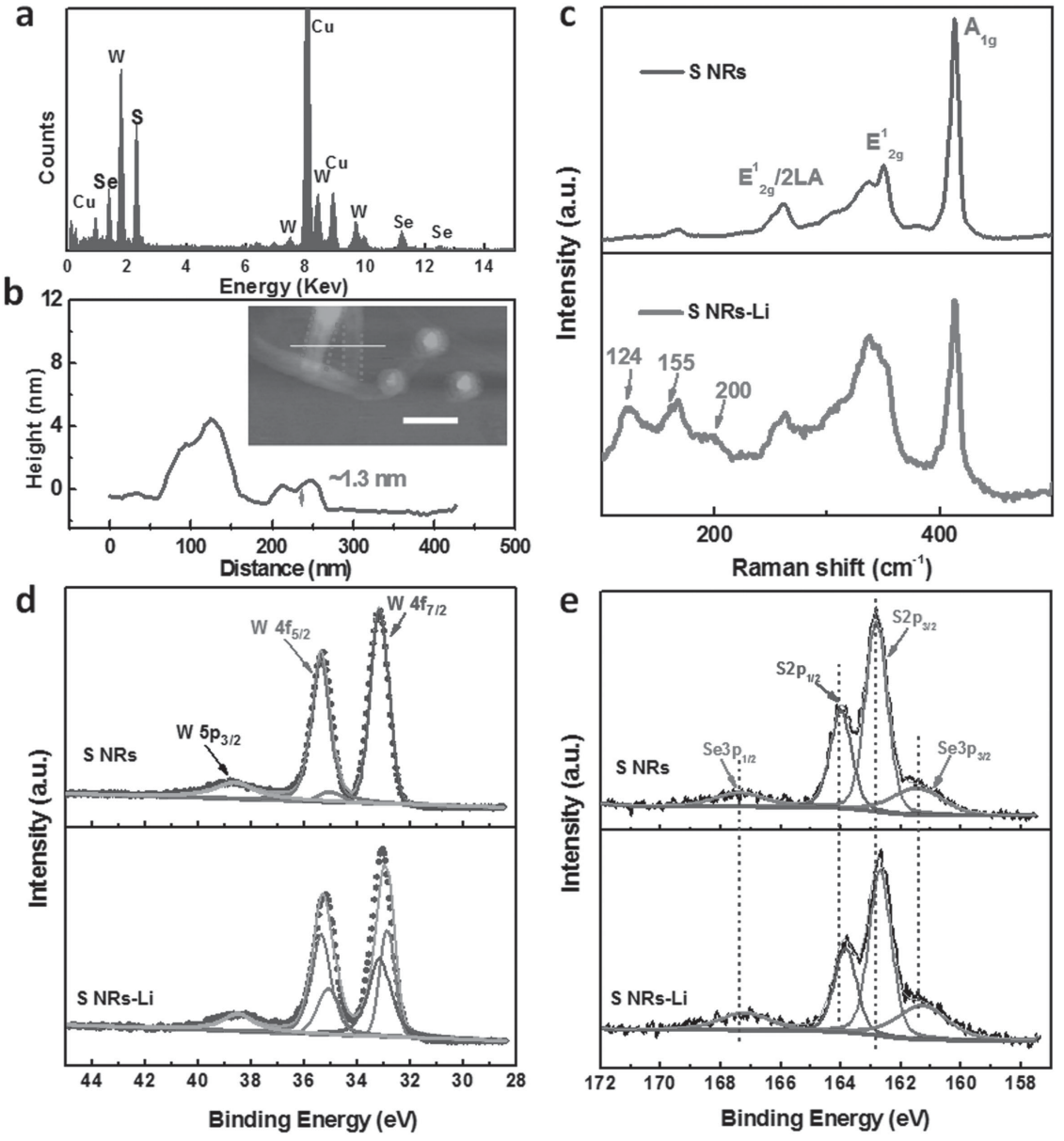

Figure 2. Characterization of $WS_{2(1-x)}Se_{2x}$ ($x \approx 0.22$) NRs after intercalation with *n*-butyl lithium. a) EDX spectrum of the ternary S NRs-Li demonstrating the atomic ratio of Se:S close to 0.44:1.56 ($x \approx 0.22$). b) AFM measurement of the corresponding S NRs-Li given the thickness of 1.3 nm, confirming the few-layered $WS_{2(1-x)}Se_{2x}$ ($x \approx 0.22$) NRs were successfully obtained. c) Raman spectra of S NRs and S NRs-Li samples. The different peaks at low frequencies (≈124, ≈155, and ≈200 cm^{-1}) are associated with the phonon modes of $WS_{2(1-x)}Se_{2x}$ contained 1T phases. Comparison of high-resolution XPS spectra of d) W4f and e) S2p regions, showing a clear shift to lower binding energies in S NRs-Li.

transferred from the conductive CFs to the NRs directly and hence decrease the resistance.

Remarkably, NRs-Li sample shows dramatically improved HER activity in **Table 1**, where the overpotential at 10 mA cm^{-2} has been shifted to about 173 mV versus RHE, which is comparable or even better than the previously reported values for metallic TMDs, such as 1T-MoS_2,[22] 1T-WS_2,[8,9] ternary $WS_{2(1-x)}Se_{2x}$ nanosheet,[33] and $MoS_{2(1-x)}Se_{2x}$.[19] By contrast, the $WS_{2(1-x)}Se_{2x}$ ($x \approx 0.22$) NTs with Li intercalation (denoted as S NTs-Li) in the same condition are also checked. The less prominent HER performance is due to the limited exposed active areas. The enhancement in catalytic activity was even more apparent upon comparison of the Tafel plots in Figure 3b. The Tafel slope after *iR* correction of ≈68 mV dec^{-1} for the S NRs-Li is lower than that of ≈77 mV dec^{-1} for S NRs, ≈78 mV dec^{-1} for S NTs-Li, and ≈84 mV dec^{-1} for S NTs, suggesting excellent kinetic behavior of ternary S NRs-Li sample. This also confirms that the Volmer–Heyrovsky mechanism reaction dominates in the hydrogen evolution.[2,34] The lower Tafel slope and earlier onset of catalytic activity, namely, the potential at which the HER activity begins, indicate the Gibbs free energy ΔG_H° is closer to equilibrium.[5,35]

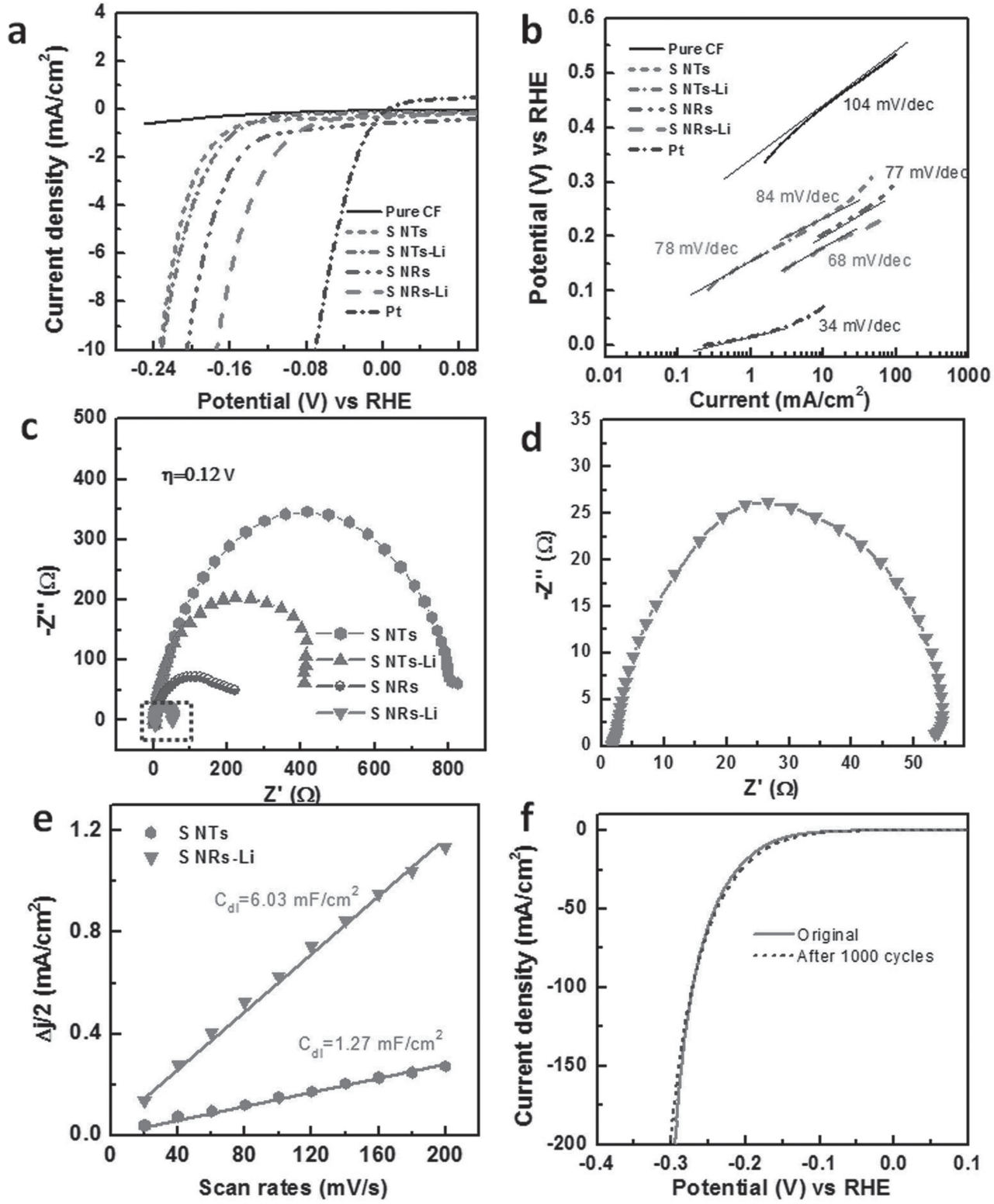

Figure 3. Comparison of the HER electrocatalytic properties of different $WS_{2(1-x)}Se_{2x}$ ($x \approx 0.22$) samples. a) Polarization curves for HER with different CF electrodes covered by $WS_{2(1-x)}Se_{2x}$ ($x \approx 0.22$) NTs (denoted as S NTs), NTs-Li (NTs after Li intercalation), NRs, NRs-Li, and a pure CF electrode. Catalyst loading is about 0.30 ± 0.02 mg cm^{-2} for all samples. Sweep rate, 5 mV s^{-1}. b) Tafel plot for the various catalysts derived from (a). c,d) EIS Nyquist plots collected at a bias voltage of –0.12 V versus RHE show the facile electrode kinetics of the different samples. e) Comparison of C_{dl} for S NTs and S NRs-Li, confirming the reserved high electrochemically active surface area of S NRs-Li. f) Stability test for HER of the S NRs-Li catalyst. Negligible HER current was lost after 1000 cycles, suggesting the superior stability of S NRs-Li in acid media.

Table 1. Comparison of electrocatalytic parameters of different ternary $WS_{2(1-x)}Se_{2x}$ catalysts.

Sample	Tafel slope [mV dec^{-1}]	Exchange current density, j_o [a] [A cm^{-2}]	η_{10} [b] [mV vs RHE [c]]	R_{ct} [d] [Ω]
S NTs	84	1.64×10^{-5}	235	≈700
S NRs	77	2.24×10^{-5}	203	≈144
S NRs-Li	68	2.50×10^{-5}	173	≈50

[a] j_o were obtained from Tafel curves using an extrapolation method; [b] η_{10}, overpotential at a current density of 10 mA cm^{-2}; [c] RHE, reversible hydrogen electrode; [d] R_{ct}, charge transfer resistance obtained from the EIS spectra.

The tensile strain on the basal plane induced by 1T phase, along with the presence of local lattice distortions, improve the ΔG_H^o on the basal plane and facilitate catalytic performance.[8] The increased exchange current density (j_0) of the S NRs-Li reveals the improved intrinsic catalytic capacity (Table 1). Additionally, electrochemical impedance spectroscopy (EIS) is utilized to investigate the electrode kinetic under the catalytic HER operating condition (Figure 3c). The small series resistance of ≈1.8 Ω (Figure 3d) for all samples ensures the importance of the direct synthesis on a conductive substrate, minimizing parasitic ohmic losses. The dramatically reduced charge transfer resistance (R_{ct} ≈ 50 Ω) for the S NRs-Li in contrast to that for S NRs (≈144 Ω) and S NTs (≈700 Ω) reveals superior kinetics toward hydrogen evolution. The high C_{dl} (6.03 mF cm^{-2}) of S NRs-Li in Figure 3e demonstrates the large electrochemically active surface area after introducing 1T phase. The local strain induced from the different surface structure, nevertheless, is vital for the outstanding HER performance. For the S NRs-Li sample, the superior HER performance is resulted from the favorable ΔG_H^o introduced from the tensile regions on the surface. And the active sites are mainly located in the basal plane.[25] Meanwhile, the few-layered NRs entwining on the surface of CFs could easily host the electron transfer from the substrate and reduce the resistance for each traversed layer.

The long-term stability of the S NRs-Li sample was assayed by taking continuous cyclic voltammetry (CV) cycles to evaluate its electrocatalytic performance. The comparison of polarization curves with *iR* correction after 1000 cycles and the original curve was displayed in Figure 3f. The nearly identical curves imply the excellent catalytic stability of S NRs-Li sample. Moreover, this sample was able to maintain a stable HER current density for ≈6 h at a constant voltage of –118 mV versus RHE in 0.5 M H_2SO_4 (Figure S8, Supporting Information). Impressively, the almost reserved morphology and no obvious chemical composition change suggest the promise for implementing this new catalyst into realistic hydrogen evolution electrode (Figure S9, Supporting Information).

3. Conclusion

In summary, the few-layered ternary $WS_{2(1-x)}Se_{2x}$ NRs with metallic phases are in situ grown on the CFs. Benefiting from the increased active edges and ultrathin layers, our ternary $WS_{2(1-x)}Se_{2x}$ NRs-Li sample exhibits a higher electrocatalytic activity in acid media than $WS_{2(1-x)}Se_{2x}$ NTs. Of particular note is that the favorable ΔG_H^o introduced from the tensile region, along with the presence of local lattice distortions, on the surface of S NRs-Li promotes the HER ($2H^+ + 2e^- \rightarrow H_2$) process. The long-term durability of S NRs-Li suggests the potential of practical applications in acid electrolytes. Our experimental results indicate that the ternary $WS_{2(1-x)}Se_{2x}$ NRs with 1T phases are a prominent alternative for platinum-based HER electrocatalysts.

4. Experimental Section

Synthesis of S NRs on CFs: All chemicals are of analytical grade and were used as received without further purification. First, WO_3 nanowires were grown on the CFs through the previously reported method[23,36] with slight modification via heating the WO_3 powder at 1020 °C in the furnace. The uniform WO_3 nanowires vertically covered the CFs as shown in Figure S1a (Supporting Information). To prepare the $WS_{2(1-x)}Se_{2x}$ NTs, the CFs with WO_3 NWs were put on the back zone in the two-zone furnace, while the certainly proportional S and Se powder (≈0.6 g, 99.8% Alfa Aesar) as precursor was in the front zone. When the temperature of the back zone was raised to 800 °C, the temperature of the front zone was quickly increased to 260 °C simultaneously.[23] The conversion process was maintained for 60 min with 50 sccm Ar gas. After the conversion process, the furnace was allowed to cool to room temperature. Then, the as-grown $WS_{2(1-x)}Se_{2x}$ NTs on CFs were immersed into an ethanol–DI water solvent (35 mL) with a volume ratio of $V_{ethanol}$:V_{DI} = 2:33 in 50 mL autoclave, which was sealed and maintained at 170 °C for 1 h. The resulting sample was washed by DI water and ethanol, respectively, and dried for next use. As comparison, the binary WS_2 and WSe_2 NRs were also prepared with the same method.

Lithium Intercalation of $WS_{2(1-x)}Se_{2x}$ NRs (S NRs-Li): As-synthesized ternary S NRs were soaked in 10 mL *n*-butyllithium (2.4 M in hexane, J&K Scientific) inside sealed vials with stirring at ≈50 °C under nitrogen atmosphere (a home-made special equipment). After 16 h, DI water was carefully added dropwise into the solution slowly and reacted with excess *n*-butyllithium under the condition of a large amount of N_2 gas flowing (Note! This reaction is dangerous and may catch fire). Then, the CFs covered with NRs were reacted with excess DI water and gently rinsed with water. Finally, the mass loading of the grown NRs on CFs is about 0.30 ± 0.02 mg cm^{-2}, determined through using an electronic balance (BT 125D) with 10 μg accuracy.

Materials Characterizations: The samples were characterized by different analytical techniques. The morphologies were observed under a Hitachi S4800 SEM equipped with an X-ray energy dispersive spectrometer (EDS) and FEI Tecnai F20 TEM operated at 200 kV. STEM-EDX elemental mapping was performed on JEM-2100F. XRD (D/MAX-TTRIII (CBO) diffractometer) using Cu Kα radiation (λ = 1.5418 Å). Raman scattering was performed on a confocal microscope–based Raman spectrometer (Renishaw InVia, 532 nm excitation laser). XPS was recorded on ESCALAB 250 Xi. The thickness was examined by AFM (Bruker Icon) by drop-casting ultrasonicated dispersion onto a silicon wafer. The pH of the electrolyte was tested on the METTLER TOLEDO pH meter (FE20).

Electrochemical Measurement: Electrochemical measurements were performed in a three-electrode system at an electrochemical station (CHI 660D). Typically, a CF sample with the test area of 0.5 cm^2 served as a working electrode using a saturated calomel electrode (SCE) as the reference electrode and a platinum wire as the counter electrode. All the potentials were calibrated to a reversible hydrogen electrode (RHE). The conversion between potentials versus SCE and versus RHE was performed using Equations (1) and (2). For comparison, the pure CF was also cleaned and dried for electrochemical measurements

$$E\,(\text{vs RHE}) = E\,(\text{vs SCE}) + E_{SCE}\,(\text{reference}) + 0.059 \times \text{pH} \quad (1)$$

where

$$E_{SCE}\,(\text{reference}) = 0.2412\ \text{V vs RHE at } 25^{\circ}\text{C} \quad (2)$$

Before the electrochemical measurement, the electrolyte (≈0.5 M H_2SO_4, pH ≈ 0.69) was purged with pure N_2 (99.999%). The polarization curves were obtained by sweeping the potential from −1.0 to 0 V versus SCE at room temperature with a sweep rate of 5 mV s^{-1}. Electrochemical impedance spectroscopy was performed when the working electrode was biased at a constant ≈0.120 V versus RHE while sweeping the frequency from 2 MHz to 10 mHz with a 10 mV AC dither. The electrochemical stability of the catalyst was evaluated by cycling the electrode 1000 times from −0.4 to 0.0 V versus SCE with a scan rate of 100 mV s^{-1}. Cyclic voltammograms taken with various scan rates (20, 40, 60, etc., mV s^{-1}) used to estimate the double-layer capacitance were collected in the 0.18–0.28 V versus RHE region. As a comparison, the pure Pt foil (99.99%) with same test area was performed with electrochemical measurement in the same condition.

Supporting Information

Supporting Information is available from the Wiley Online Library or from the author.

Acknowledgements

This work at National Center for Nanoscience and Technology was supported by 973 Program of the Ministry of Science and Technology of China (No. 2012CB934103), the 100-Talents Program of the Chinese Academy of Sciences (No. Y1172911ZX), the National Natural Science Foundation of China (Nos. 21373065 and 61474033), and Beijing Natural Science Foundation (No. 2144059). The authors gratefully acknowledge the support of K.C. Wong Education Foundation.

Received: July 1, 2015
Revised: August 10, 2015
Published online: September 9, 2015

[1] a) A. J. Nozik, J. Miller, *J. Chem. Rev.* **2010**, *110*, 6443; b) M. R. Gao, J. X. Liang, Y. R. Zheng, Y. F. Xu, J. Jiang, Q. Gao, J. Li, S.-H. Yu, *Nat. Commun.* **2015**, *6*, 5982; c) X. Huang, Z. Zeng, H. Zhang, *Chem. Soc. Rev.* **2013**, *42*, 1934.
[2] B. E. Conway, B. V. Tilak, *Electrochim. Acta* **2002**, *47*, 3571.
[3] B. Hinnemann, P. G. Moses, J. Bonde, K. P. Jørgensen, J. H. Nielsen, S. Horch, I. Chorkendorff, J. K. Nørskov, *J. Am. Chem. Soc.* **2005**, *127*, 5308.
[4] a) M. Chhowalla, H. S. Shin, G. Eda, L.-J. Li, K. P. Loh, H. Zhang, *Nat. Chem.* **2013**, *5*, 263; b) Y. Yan, B. Xia, Z. Xu, X. Wang, *ACS Catal.* **2014**, *4*, 1693.
[5] J. D. Benck, T. R. Hellstern, J. Kibsgaard, P. Chakthranont, T. F. Jaramillo, *ACS Catal.* **2014**, *4*, 3957.
[6] a) J. V. Lauritsen, J. Kibsgaard, S. Helveg, H. Topsoe, B. S. Clausen, E. Laegsgaard, F. Besenbacher, *Nat. Nanotechnol.* **2007**, *2*, 53; b) T. F. Jaramillo, K. P. Jørgensen, J. Bonde, J. H. Nielsen, S. Horch, I. Chorkendorff, *Science* **2007**, *317*, 100.
[7] J. Xie, H. Zhang, S. Li, R. Wang, X. Sun, M. Zhou, J. Zhou, X. W. Lou, Y. Xie, *Adv. Mater.* **2013**, *25*, 5807.
[8] D. Voiry, H. Yamaguchi, J. Li, R. Silva, D. C. B. Alves, T. Fujita, M. Chen, T. Asefa, V. B. Shenoy, G. Eda, M. Chhowalla, *Nat. Mater.* **2013**, *12*, 850.
[9] M. A. Lukowski, A. S. Daniel, C. R. English, F. Meng, A. Forticaux, R. J. Hamers, S. Jin, *Energy Environ. Sci.* **2014**, *7*, 2608.
[10] Y. Jung, J. Shen, Y. Liu, J. M. Woods, Y. Sun, J. J. Cha, *Nano Lett.* **2014**, *14*, 6842.
[11] D. Kong, H. Wang, J. J. Cha, M. Pasta, K. J. Koski, J. Yao, Y. Cui, *Nano Lett.* **2013**, *13*, 1341.
[12] H. Wang, D. Kong, P. Johanes, J. J. Cha, G. Zheng, K. Yan, N. Liu, Y. Cui, *Nano Lett.* **2013**, *13*, 3426.
[13] A. Y. S. Eng, A. Ambrosi, Z. Sofer, P. Šimek, M. Pumera, *ACS Nano* **2014**, *8*, 12185.
[14] S. Mao, Z. Wen, S. Ci, X. Guo, K. Ostrikov, J. Chen, *Small* **2015**, *11*, 414.
[15] J. Xie, J. Zhang, S. Li, F. Grote, X. Zhang, H. Zhang, R. Wang, Y. Lei, B. Pan, Y. Xie, *J. Am. Chem. Soc.* **2013**, *135*, 17881.
[16] a) N. Liu, P. Kim, J. H. Kim, J. H. Ye, S. Kim, C. J. Lee, *ACS Nano* **2014**, *8*, 6902; b) M. S. Faber, S. Jin, *Energy Environ. Sci.* **2014**, *7*, 3519.
[17] D. Merki, H. Vrubel, L. Rovelli, S. Fierro, X. Hu, *Chem. Sci.* **2012**, *3*, 2515.
[18] J. Bonde, P. G. Moses, T. F. Jaramillo, J. K. Norskov, I. Chorkendorff, *Faraday Discuss.* **2009**, *140*, 219.
[19] V. Kiran, D. Mukherjee, R. N. Jenjeti, S. Sampath, *Nanoscale* **2014**, *6*, 12856.
[20] C. Xu, S. Peng, C. Tan, H. Ang, H. Tan, H. Zhang, Q. Yan, *J. Mater. Chem. A* **2014**, *2*, 5597.
[21] X. Zhang, F. Meng, S. Mao, Q. Ding, M. J. Shearer, M. S. Faber, J. Chen, R. J. Hamers, S. Jin, *Energy Environ. Sci.* **2015**, *8*, 862.
[22] M. A. Lukowski, A. S. Daniel, F. Meng, A. Forticaux, L. Li, S. Jin, *J. Am. Chem. Soc.* **2013**, *135*, 10274.
[23] K. Xu, F. Wang, Z. Wang, X. Zhan, Q. Wang, Z. Cheng, M. Safdar, J. He, *ACS Nano* **2014**, *8*, 8468.
[24] J. J. Hu, J. S. Zabinski, J. E. Bultman, J. H. Sanders, A. A. Voevodin, *Tribol. Lett.* **2006**, *24*, 127.
[25] D. Voiry, M. Salehi, R. Silva, T. Fujita, M. Chen, T. Asefa, V. B. Shenoy, G. Eda, M. Chhowalla, *Nano Lett.* **2013**, *13*, 6222.
[26] a) M. Kertesz, R. Hoffmann, *J. Am. Chem. Soc.* **1984**, *106*, 3453; b) M. A. Py, R. R. Haering, *Can. J. Phys.* **1983**, *61*, 76.
[27] H.-L. Tsai, J. Heising, J. L. Schindler, C. R. Kannewurf, M. G. Kanatzidis, *Chem. Mater.* **1997**, *9*, 879.
[28] W. Zhao, Z. Ghorannevis, K. K. Amara, J. R. Pang, M. Toh, X. Zhang, C. Kloc, P. H. Tan, G. Eda, *Nanoscale* **2013**, *5*, 9677.
[29] S. Jiménez Sandoval, D. Yang, R. Frindt, J. Irwin, *Phys. Rev. B* **1991**, *44*, 3955.
[30] Y. Yang, H. Fei, G. Ruan, C. Xiang, J. M. Tour, *Adv. Mater.* **2014**, *26*, 8163.
[31] Y. Zheng, Y. Jiao, M. Jaroniec, S. Z. Qiao, *Angew. Chem. Int. Ed.* **2015**, *54*, 52.
[32] H. Wang, Q. Zhang, H. Yao, Z. Liang, H.-W. Lee, P.-C. Hsu, G. Zheng, Y. Cui, *Nano Lett.* **2014**, *14*, 7138.
[33] Q. Fu, L. Yang, W. Wang, A. Han, J. Huang, P. Du, Z. Fan, J. Zhang, B. Xiang, *Adv. Mater.* **2015**, *27*, 4732.
[34] Y. Li, H. Wang, L. Xie, Y. Liang, G. Hong, H. Dai, *J. Am. Chem. Soc.* **2011**, *133*, 7296.
[35] A. B. Laursen, S. Kegnaes, S. Dahl, I. Chorkendorff, *Energy Environ. Sci.* **2012**, *5*, 5577.
[36] F. Wang, Y. Wang, X. Zhan, M. Safdar, J. Gong, J. He, *CrystEngComm* **2014**, *16*, 1389.